Temporal evolution of surface ripples on a finite plasma slab subject to the magneto-Rayleigh-Taylor instability

M. R. Weis,[1] P. Zhang,[1] Y. Y. Lau,[1,a)] I. M. Rittersdorf,[1,b)] J. C. Zier,[1,c)] R. M. Gilgenbach,[1] M. H. Hess,[2] and K. J. Peterson[2]

[1]*Department of Nuclear Engineering and Radiological Sciences, University of Michigan, Ann Arbor, Michigan 48109-2104, USA*
[2]*Sandia National Laboratories, Albuquerque, New Mexico 87185, USA*

Using the ideal magnetohydrodynamic model, we calculate the temporal evolution of initial ripples on the boundaries of a planar plasma slab that is subjected to the magneto-Rayleigh-Taylor instability. The plasma slab consists of three regions. We assume that in each region the plasma density is constant with an arbitrary value and the magnetic field is also constant with an arbitrary magnitude and an arbitrary direction parallel to the interfaces. Thus, the instability may be driven by a combination of magnetic pressure and kinetic pressure. The general dispersion relation is derived, together with the feedthrough factor between the two interfaces. The temporal evolution is constructed from the superposition of the eigenmodes. Previously established results are recovered in the various limits. Numerical examples are given on the temporal evolution of ripples on the interfaces of the finite plasma slab. © *2014 AIP Publishing LLC.*
[http://dx.doi.org/10.1063/1.4904210]

I. INTRODUCTION

Magneto-Rayleigh-Taylor instability (MRT)[1–12] is important to magnetized target fusion,[13–16] wire-array Z-pinches,[17–21] and equation-of-state studies using flyer plates[22,23] or isentropic compression.[24] It is also important to the study of the crab nebulae.[25] The magnetized liner inertial fusion (MagLIF) concept, recently proposed at Sandia National Laboratories,[26–31] utilizes magnetic compression of a cylindrical, metal liner to adiabatically compress a laser-generated plasma. This plasma is preheated and embedded in an axial magnetic field. The primary concern in this concept is MRT that could disrupt the symmetry of the implosion.[30,31] This paper addresses several MRT properties that could be important to the MagLIF concept but have not been sufficiently treated analytically. In particular, we focus on liner implosions, which may be treated as magnetically accelerated flyer plates for large enough radius.

A general feature in MagLIF is the simultaneous presence of plasma and of magnetic fields with different orientations and magnitudes in the different regions (fuel, liner, and vacuum), both inside the liner and exterior to the liner. The outer surface of the liner is MRT unstable during the initial phase of implosion, and the MRT is driven by the azimuthal magnetic field that is produced by the liner's axial current. In the final stage implosion, which is designed to be high beta, the inner interface of the liner becomes classically Rayleigh-Taylor (RT) unstable due to deceleration,[32] a result of the increasing plasma pressure in the fusion fuel. Thus, during the implosion, there is a conversion from magnetic pressure driven to kinetic pressure driven instabilities. The effect of magnetic tension, $\sim (\boldsymbol{k} \cdot \boldsymbol{B})^2$, will enter differently at the different stages of implosion. A highly compressed axial field may inhibit growth of axial modes on the inner surface, while significant diffusion of the drive field could stabilize non-axisymmetric modes. In both cases, $(\boldsymbol{k} \cdot \boldsymbol{B})^2$ could be large. In addition, the direction of the effective gravity, g, changes sign as the liner stagnates on hot fuel. In a recent MagLIF experiment on a cylindrical liner, Awe *et al.*[30,31] found evidence that an embedded axial magnetic field may have strengthened the integrity of the inner liner surface against MRT. It is possible that the compressed axial magnetic field might have reduced the feedthrough factor from the liner's outer surface to the liner's inner surface.[8,30,31] Section V will address some possible evidence of this from 2D simulations.

The feedthrough factor measures the effect of perturbation at one interface on the other interface.[8,32,33] For the most unstable eigenmode of MRT, it may be taken as the ratio of the perturbation displacements at the two interfaces that are obtained from the unstable mode's eigenfunction.[1,8] The MRT developed initially on the outer liner surface may therefore "feedthrough" to the inner interface. This feedthrough could provide significant seeding for instability growth at the inner interface when the implosion is slowed down radially by the increasing pressure in the fusion fuel, as mentioned in the preceding paragraph. The feedthrough factor may be substantially reduced if the MRT perturbations that were initiated from the outer surface cause significant bending of a strong magnetic field at the inner surface.[8]

---

a)Author to whom correspondence should be addressed. Electronic mail: yylau@umich.edu
b)Now holding a National Research Council Research Associateship Award at Naval Research Laboratory, Washington, DC 20375, USA.
c)Now with the Plasma Physics Division, Naval Research Laboratory, Washington, DC 20375, USA.

In this paper, we construct the closed-form solution for the evolution of surface ripples, over a finite time interval, on a finite plasma slab using a WKBJ approach. MRT is driven by an arbitrary combination of magnetic pressure and fluid pressure. In each region of the finite plasma slab, including its adjoining regions, the density may be arbitrary and the magnetic field may have an arbitrary amplitude and an arbitrary direction parallel to the interfaces. To potentially account for the effect of a compressed magnetic field, we generalize our previous work[8] and assume that the plasma is bounded by rigid, perfect conductors, as shown in Fig. 1. Thus, the finite widths of regions I and III (h_1 and h_3 in Fig. 1) may vary adiabatically. This model is a substantial generalization of the classical papers by Taylor,[32] Kruskal and Schwartzschild,[2] Chandrasekhar,[3] and Harris.[1] A general dispersion relation for the geometry shown in Fig. 1 is obtained, together with the feedthrough factors. From these solutions, we integrate analytic solutions for the temporal evolution of the initial ripples on both interfaces, and the mutual interaction between them.

The closed form solution for arbitrary magnetic field, plasma density, and kinetic pressure may be used to assess qualitatively the severity of MRT once the temporal evolution of these equilibrium quantities are given (from numerical codes, experiments, or test case studies). As the equilibrium evolves, the MRT growth and feedthrough also evolve accordingly. The WKBJ technique then provides an accurate evaluation of the temporal evolution of the surface ripples on both interfaces, under the customary assumption that the equilibrium evolves on a time scale longer than the e-folding time of the instantaneous MRT growth[7] and the ripple amplitude remains small so that growth remains linear. We present numerical examples on the temporal evolution of the surface ripples under these assumptions, using the equilibrium profile that is extracted from the simulation code, HYDRA.[34] These examples are related to the MRT experiments by Sinars *et al.*[7] and Awe *et al.*[30,31]

The basic assumptions of this work follow: (1) It is an ideal magnetohydrodynamic (MHD) model, and the fluid is incompressible. (2) It is a linear theory. (3) It applies to

a Cartesian slab, so that the kink (m = 1) and sausage mode (m = 0) MHD instabilities, and the Bell-Plesset effects[35,36]—all due to cylindrical geometry—are absent. (4) It is a sharp boundary model, in which both the plasma density and the magnetic field are constant and uniform within each region (Fig. 1). (5) The plasma slab may have a finite width in each region. On the outer boundaries, the plasma is in contact with a rigid, perfect conductor.

In Sec. II, we describe the equilibrium model. We derive the general dispersion relation from the second order ordinary differential equation in Sec. III. An alternate derivation using pressure balance is given in the Appendix A. In Sec. IV, the temporal evolution of the ripples is calculated. In Sec. V, we present the numerical examples. Concluding remarks are given in Sec. VI. Some limiting cases of Fig. 1 are summarized in Appendix B, where we demonstrate how such limits may be deduced from the general dispersion relation. These limits include various combinations of $h_1 \to \infty$, $h_3 \to \infty$, $\Delta \to \infty$, $\rho_{01} \to 0$, $\rho_{02} \to 0$, and $\rho_{03} \to 0$ in Fig. 1.

II. EQUILIBRIUM

We begin with a general equilibrium of a magnetized plasma whose mass density, fluid velocity, and magnetic field are given by[37]

$$\rho_0 = \rho_0(x), \tag{1}$$

$$\mathbf{v}_0 = \mathbf{v}_0(x) = 0, \tag{2}$$

$$\mathbf{B}_0 = B_{y0}(x)\hat{y} + B_{z0}(x)\hat{z}. \tag{3}$$

By writing Eq. (2), we consider the rest frame of the plasma, in the event that this plasma is under constant acceleration in the lab frame. The kinetic (fluid) pressure, p_0, and magnetic pressure, p_{m0}, also vary with x,

$$p_0 = p_0(x), \tag{4}$$

$$p_{m0} = p_{m0}(x) = \frac{|\mathbf{B}_0(x)|^2}{2\mu_0} \equiv \frac{B_0^2(x)}{2\mu_0}. \tag{5}$$

The x-dependence of ρ_0, $\mathbf{B}_0$, and p_0 is arbitrary; they only need to satisfy the equilibrium condition, for all x (Ref. 37)

$$\frac{\partial}{\partial x}\left(p_0(x) + \frac{B_0^2(x)}{2\mu_0}\right) = -\rho_0(x)g. \tag{6}$$

Equation (6) states that the acceleration in the lab frame, $a = -g$, may be driven by either the kinetic pressure, or magnetic pressure, or a combination of the two. In this paper, we assume that g is a constant that satisfies Eq. (6). Integration of Eq. (6) from x_1 to x_2 ($>x_1$) yields

$$\left(p_0(x_2) + \frac{B_0^2(x_2)}{2\mu_0}\right) - \left(p_0(x_1) + \frac{B_0^2(x_1)}{2\mu_0}\right) = -\int_{x_1}^{x_2} dx\,\rho_0(x)g. \tag{7}$$

In the sharp boundary model, shown in Fig. 1, there are three regions, I ($\mu < x < \beta$), II ($\beta < x < \alpha$), and III
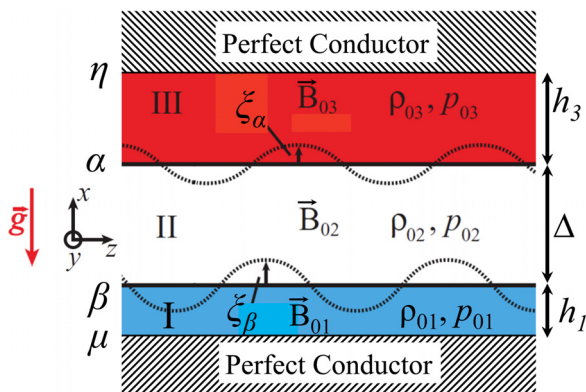

FIG. 1. MRT model with two interfaces at $x = \alpha$ and at $x = \beta$. The bottom boundary of region I ($x = \mu$) and the top boundary of region III ($x = \eta$) are in contact with a rigid, perfect conductor.

($\alpha < x < \eta$). Within each region, both density ρ_{0i} and magnetic field $\mathbf{B}_{0i}$ are constant and uniform, where i = 1, 2, and 3. The widths of the three regions are h_1, Δ, and h_3, as shown in Fig. 1; each of which may assume an arbitrary value from zero to arbitrarily large. On the outer boundaries, at $x = \mu$ and at $x = \eta$, the plasma is in contact with a rigid, perfect conductor. Setting $x_1 = \beta^-$ and to $x_2 = \alpha^+$ in Eq. (7), we obtain

$$g\rho_{02}\Delta = \left[p_0(\beta^-) + \frac{B_{01}^2}{2\mu_0}\right] - \left[p_0(\alpha^+) + \frac{B_{03}^2}{2\mu_0}\right], \quad (8)$$

where $B_{0i} = |\mathbf{B}_{0i}|$, α^+ (α^-) denotes the location slightly above (below) $x = \alpha$, with a similar designation for β^+ and β^- at $x = \beta$, and $\Delta = \alpha - \beta$. Equation (8) states that the weight in region II is supported by the total pressure difference between the two interfaces, α and β [Fig. 1]. Across the α- and β-interfaces, we have, from Eq. (7),

$$p_0(\alpha^+) + \frac{B_{03}^2}{2\mu_0} = p_0(\alpha^-) + \frac{B_{02}^2}{2\mu_0}, \quad (9)$$

$$p_0(\beta^+) + \frac{B_{02}^2}{2\mu_0} = p_0(\beta^-) + \frac{B_{01}^2}{2\mu_0}. \quad (10)$$

These two equations state that the total pressure is continuous across an interface. Equations (8)–(10) describe various types of equilibrium, briefly reviewed below.

When the upper boundary α is sufficiently far away from the lower boundary β, Eq. (10) is the equilibrium condition for the interface β. For the classical RT model, in which a heavy fluid sets on a light fluid without any magnetic field, Eq. (10) becomes

$$p_0(\beta^+) = p_0(\beta^-). \quad (11)$$

For the single interface problem considered by Chandrasekar,[3] Kruskal and Schwartzchild,[2] the upper-half space could be magnetic field-free; whereas the lower half space is vacuum filled with a magnetic field. Equation (10) becomes

$$p_0(\beta^+) = \frac{B_{01}^2}{2\mu_0}, \quad (12)$$

showing the weight being supported by the vacuum magnetic field below. In Harris' two-interface slab model,[1] the equilibrium consists of $B_{02} = B_{03} = 0$, $\rho_{01} = \rho_{03} = 0$ so that the weight in region II is supported by the vacuum magnetic field B_{01} in region I. The equilibrium condition Eq. (8) reduces to

$$g\rho_{02}\Delta = \frac{B_{01}^2}{2\mu_0}, \quad (13)$$

which directly links the gravity to the magnetic pressure that drives MRT. In Harris' analysis of MRT,[1] the effects of magnetic field (specifically the bending of magnetic field line) became entangled with the gravity after he eliminated

B_{01} using Eq. (13). Thus, the difference between fluid pressure driven or magnetic pressure driven was masked in Harris' treatment.[8] Finally, if the magnetic field is discontinuous at the α-interface, there is a surface current at that interface, whose y- and z-components, $K_{0y\alpha}$ and $K_{0z\alpha}$, respectively, are given by

$$K_{0y\alpha} = -[B_{0z}(\alpha^+) - B_{0z}(\alpha^-)]/\mu_0,$$
$$K_{0z\alpha} = [B_{0y}(\alpha^+) - B_{0y}(\alpha^-)]/\mu_0. \quad (14)$$

Replacing α with β, Eq. (14) gives the surface current at the β-interface.

Hereafter, we assume that the gravity, g, is an independent, pre-assigned constant which may be positive, negative, or zero. The gravitational weight is supported either by the fluid pressure or by the magnetic pressure, or by an arbitrary combination of the two. The only requirement is that the general equilibrium condition, Eq. (8), is satisfied. Equations (11)–(13) describe the specific equilibrium commonly treated in the literature; their stability analysis is summarized in Appendix B.

III. PERTURBATION AND DISPERSION RELATION

We first consider a small signal perturbation on a general equilibrium modeled by Eqs. (1)–(6). We assume that the fluid is incompressible and is governed by the ideal MHD equations: $\rho(\partial/\partial t + \mathbf{v} \cdot \nabla)\mathbf{v} = -\nabla_p + \mathbf{J} \times \mathbf{B} - \rho g\mathbf{x}$, $\partial\rho/\partial t + \nabla \cdot (\rho\mathbf{v}) = 0$, $\nabla \cdot \mathbf{v} = 0$, $\partial\mathbf{B}/\partial t = \nabla \times (\mathbf{v} \times \mathbf{B})$, and $\nabla \times \mathbf{B} = \mu_0\mathbf{J}$. The total fluid pressure, the total fluid velocity, and the total magnetic field, for instance, are written in the form

$$p = p_0(x) + p_1(x)e^{i\omega t - ik_y y - ik_z z},$$
$$\mathbf{v} = \mathbf{v}_0 + \mathbf{v}_1 = \mathbf{v}_1 \equiv i\omega\boldsymbol{\xi}_1$$
$$= i\omega[\xi_{1x}(x), \xi_{1y}(x), \xi_{1z}(x)]e^{i\omega t - ik_y y - ik_z z},$$
$$\mathbf{B} = \mathbf{B}_0 + \mathbf{B}_1 = \mathbf{B}_0 + [B_{1x}(x), B_{1y}(x), B_{1z}(x)]e^{i\omega t - ik_y y - ik_z z},$$
$$(15)$$

where quantities with a subscript 1 are small signal quantities, and the equilibrium quantities, designated with a subscript 0, satisfy Eqs. (1)–(6). In Eq. (15), the perturbation velocity, $\mathbf{v}_1$, is written in terms of the perturbation displacement whose three components are ξ_{1x}, ξ_{1y}, and ξ_{1z}. The most important perturbation quantity is ξ_{1x}, the x-component of the fluid displacement (Fig. 1). By linearizing the ideal MHD equations, one finds that ξ_{1x} is governed by the eigenvalue equation[3,37]

$$\frac{\partial}{\partial x}\left\{\left[-\omega^2\rho_0 + \frac{(\mathbf{k} \cdot \mathbf{B}_0)^2}{\mu_0}\right]\frac{\partial\xi_{1x}}{\partial x}\right\}$$
$$= k^2\left[-\omega^2\rho_0 - g\frac{\partial\rho_0}{\partial x} + \frac{(\mathbf{k} \cdot \mathbf{B}_0)^2}{\mu_0}\right]\xi_{1x}, \quad (16)$$

$$\mathbf{k} = k_y\hat{y} + k_z\hat{z}, \quad k = |\mathbf{k}| = \sqrt{k_y^2 + k_z^2}. \quad (17)$$

Equation (16) is the governing equation for all equilibrium profiles that satisfy Eqs. (1)–(6). We have recently studied the effects of magnetic shear on MRT,[12] using Eq. (16).

We now consider the sharp boundary, 3-region model of Fig. 1. We further assume that, within each region, the density ρ_0 and magnetic field $\mathbf{B}_0$ are constant and uniform. Thus, within each region, $\partial \rho_0 / \partial x = 0$, and Eq. (16) reduces to the simple equation

$$\frac{d^2 \xi_{1x}(x)}{dx^2} - k^2 \xi_{1x}(x) = 0. \tag{18}$$

It should be noted that the assumption of uniform material density in the slab configuration is only an approximation, which allows the problem to be analytically tractable (the assumption of uniform density and incompressibility will be addressed in our HYDRA simulation in Sec. V below, and in greater details in a separate paper that treats shock-induced feedthrough). If $\xi_\alpha \equiv \xi_{1x}(\alpha)$ and $\xi_\beta \equiv \xi_{1x}(\beta)$ designate, respectively, the displacement at the α-interface and the β-interface [Fig. 1], the solution to Eq. (18) in terms of ξ_α and ξ_β for the three regions is, by inspection,[38]

$$\xi_{1x}(x) = \xi_\beta \frac{\sinh k(x - \mu)}{\sinh k(\beta - \mu)}, \quad \mu < x < \beta \,(\text{region I}), \tag{19a}$$

$$\xi_{1x}(x) = \xi_\alpha \frac{\sinh k(x - \beta)}{\sinh k\Delta} - \xi_\beta \frac{\sinh k(x - \alpha)}{\sinh k\Delta},$$
$$\beta < x < \alpha \,(\text{region II}), \tag{19b}$$

$$\xi_{1x}(x) = \xi_\alpha \frac{\sinh k(x - \eta)}{\sinh k(\alpha - \eta)}, \quad \alpha < x < \eta \,(\text{region III}). \tag{19c}$$

In Eq. (19b), $\Delta = \alpha - \beta$ is the width of region II. It is easy to see from Eqs. (19a) and (19c) that $\xi_{1x} = 0$ at $x = \mu$ and at $x = \eta$, where there is a rigid boundary (Fig. 1). Clearly, ξ_{1x} is continuous at $x = \alpha$ and at $x = \beta$ in solution (19b).

There are two methods to obtain the dispersion relation for the sharp boundary model shown in Fig. 1. In the first method, which is presented in the main text, we use solution (19) and integrate Eq. (16) across the α-interface to obtain an algebraic relation between ξ_α and ξ_β. A similar algebraic relation between ξ_α and ξ_β is obtained by integrating Eq. (16) across the β-interface. For these two relations to yield nontrivial solutions of ξ_α and ξ_β, the dispersion relation for ω is obtained. In the second method,[38] which is presented in Appendix A, we express all perturbation quantities, such as $p_1(x)$ and $\mathbf{B}_1(x)$, in terms of ξ_{1x} within each region. The total perturbation pressure within each region may then be expressed in terms ξ_α and ξ_β upon using Eq. (19). Continuity of the total perturbation pressure across the α- and β-interface then give two algebraic equations in two unknowns, ξ_α and ξ_β, from which the dispersion relation follows. We have verified that these two methods yield identical results. The first method is more straightforward mathematically. The second method is more cumbersome, but is more appealing physically, as all relevant perturbation quantities are expressed in terms of $\xi_{1x}(x)$ within each region.[38]

For the first method, we integrate Eq. (16) across the α-interface to yield

$$\left\{ \left[-\omega^2 \rho_0 + \frac{(\mathbf{k} \cdot \mathbf{B}_0)^2}{\mu_0} \right] \frac{\partial \xi_{1x}}{\partial x} \right\} \Bigg|_{x=\alpha^-}^{x=\alpha^+} = -k^2 g \rho_0 \xi_{1x} |_{x=\alpha^-}^{x=\alpha^+}. \tag{20}$$

Upon using Eqs. (19b) and (19c) for $\xi_{1x}(x)$, and the respective equilibrium density ρ_0 and magnetic field $\mathbf{B}_0$ at α^+ and α^-, Eq. (20) gives the following relation between ξ_α / ξ_β,

$$\xi_\alpha / \xi_\beta = 1 \Bigg/ \left[\cosh k\Delta + \frac{\left((\mathbf{k} \cdot \mathbf{B}_{03})^2 / \mu_0 - \omega^2 \rho_{03} \right) \coth k h_3 + k g (\rho_{02} - \rho_{03})}{(\mathbf{k} \cdot \mathbf{B}_{02})^2 / \mu_0 - \omega^2 \rho_{02}} \sinh k\Delta \right] \equiv F_\alpha(\omega). \tag{21}$$

Note that $F_a(\omega)$ is the feedthrough factor from the β-interface to the α-interface.[8] Physically, $F_a(\omega)$ gives the ripple amplitude at the α-interface when the MRT *mode* produces a ripple of unit amplitude at the β-interface (Fig. 1). Likewise, upon using Eqs. (19a) and (19b) for $\xi_{1x}(x)$, and the respective equilibrium density ρ_0 and magnetic field $\mathbf{B}_0$ at β^+ and β^-, Eq. (20) with α replaced by β yields another relation for the feedthrough factor, ξ_α / ξ_β,

$$\xi_\alpha / \xi_\beta = \cosh k\Delta + \frac{\left((\mathbf{k} \cdot \mathbf{B}_{01})^2 / \mu_0 - \omega^2 \rho_{01} \right) \coth k h_1 + k g (\rho_{01} - \rho_{02})}{(\mathbf{k} \cdot \mathbf{B}_{02})^2 / \mu_0 - \omega^2 \rho_{02}} \sinh k\Delta \equiv F_b(\omega). \tag{22}$$

For Eq. (21) to be consistent with Eq. (22), we obtain the dispersion relation

$$F_\alpha(\omega) = F_b(\omega), \tag{23}$$

which may be expanded out into a second degree polynomial in ω^2,

$$A\omega^4 - B\omega^2 + C = 0, \tag{24}$$

$$A = 1 + \frac{\rho_{01}}{\rho_{02}} \frac{\rho_{03}}{\rho_{02}} \coth k h_1 \coth k h_3$$
$$+ \left(\frac{\rho_{01}}{\rho_{02}} \coth k h_1 + \frac{\rho_{03}}{\rho_{02}} \coth k h_3 \right) \coth k\Delta, \tag{25}$$

$$B = 2(\mathbf{k} \cdot \mathbf{V}_{A2})^2 + \frac{\rho_{01}}{\rho_{02}} \left[\left((\mathbf{k} \cdot \mathbf{V}_{A1})^2 + (\mathbf{k} \cdot \mathbf{V}_{A2})^2 \right) \coth k\Delta \coth kh_1 + kg(\coth kh_1 + \coth k\Delta) \right]$$
$$+ \frac{\rho_{03}}{\rho_{02}} \left[\left((\mathbf{k} \cdot \mathbf{V}_{A2})^2 + (\mathbf{k} \cdot \mathbf{V}_{A3})^2 \right) \coth k\Delta \coth kh_3 - kg(\coth kh_3 + \coth k\Delta) \right]$$
$$+ \frac{\rho_{01}}{\rho_{02}} \frac{\rho_{03}}{\rho_{02}} \left[\left((\mathbf{k} \cdot \mathbf{V}_{A1})^2 + (\mathbf{k} \cdot \mathbf{V}_{A3})^2 \right) \coth kh_1 \coth kh_3 + kg(\coth kh_3 - \coth kh_1) \right], \tag{26}$$

$$C = \left[(\mathbf{k} \cdot \mathbf{V}_{A2})^4 - (kg)^2 \right] + \frac{\rho_{01}}{\rho_{02}} \left[\left((\mathbf{k} \cdot \mathbf{V}_{A1})^2 \coth kh_1 + kg \right) \left((\mathbf{k} \cdot \mathbf{V}_{A2})^2 \coth k\Delta + kg \right) \right]$$
$$+ \frac{\rho_{03}}{\rho_{02}} \left[\left((\mathbf{k} \cdot \mathbf{V}_{A2})^2 \coth k\Delta - kg \right) \left((\mathbf{k} \cdot \mathbf{V}_{A3})^2 \coth kh_3 - kg \right) \right]$$
$$+ \frac{\rho_{01}}{\rho_{02}} \frac{\rho_{03}}{\rho_{02}} \left[\left((\mathbf{k} \cdot \mathbf{V}_{A1})^2 \coth kh_1 + kg \right) \left((\mathbf{k} \cdot \mathbf{V}_{A3})^2 \coth kh_3 - kg \right) \right], \tag{27}$$

where $\mathbf{V}_{Ai} = \mathbf{B}_{0i}/\sqrt{\mu_0 \rho_{0i}}$ is the Alfven velocity in region i, $i = 1, 2, 3$. Note that $\rho_{0i}(\mathbf{k} \cdot \mathbf{V}_{Ai})^2 = (\mathbf{k} \cdot \mathbf{B}_{0i})^2/\mu_0$ has a finite limit even if $\rho_{0i} \to 0$.

The solution to Eq. (24) gives the eigenfrequency ω,

$$\omega^2 = \frac{1}{2A} \left(B \pm \sqrt{B^2 - 4AC} \right). \tag{28}$$

In the ideal MHD description of the Rayleigh-Taylor instability, ω^2 is always real according to the energy principle.[3,37] Therefore,

$$B^2 - 4AC \geq 0, \tag{29}$$

regardless of the value (or sign) of g, $\mathbf{B}_{01}$, $\mathbf{B}_{02}$, $\mathbf{B}_{03}$, ρ_{01}, ρ_{02}, ρ_{03}, k_y, k_z, Δ, h_1, and h_3. Instability arises if $\omega^2 < 0$ in Eq. (28). Since A is always positive definite from Eq. (25), an instability always occurs if

$$C < 0, \tag{30}$$

regardless of the sign of B because at least one root of Eq. (28) satisfies $\omega^2 < 0$. If $B > 0$, the inequality of Eq. (30) is the necessary and sufficient condition for MRT instability to occur, according to Eq. (28). We shall henceforth denote ω_1 the root of the most unstable mode. The other three roots of Eq. (24) satisfy

$$\omega_2 = -\omega_1, \quad \omega_4 = -\omega_3, \tag{31}$$

since the dispersion relation Eq. (24) is a function of ω^2. In Eq. (28), ω_1^2 and ω_3^2 correspond to the minus and plus sign, respectively. Thus, the eigenfrequencies of the modes always appear in positive and negative ($\pm$) pairs, as shown in Eq. (31). Every eigenfrequency ω is either real or imaginary. The marginal stability condition is given by $\omega = 0$, at which ω^2 transitions from a positive to a negative value.[3,37]

IV. FEEDTHROUGH FACTOR AND TEMPORAL EVOLUTION OF INITIAL SURFACE PERTURBATIONS

When a slab of fluid is accelerated in vacuum, one surface is RT unstable and the other surface is RT stable,

intuitively. Consider, for example, $\rho_{01} = \rho_{03} = 0$, $h_1 = h_3 \to \infty$, and g points downward as in Fig. 1. Then the β-interface is thought to be unstable and the α-interface is thought to be stable. However, in the treatment of *eigenmodes*, ripples on both surfaces would grow at the same temporal factor, $\exp(i\omega_1 t)$, where ω_1 is the eigenfrequency with the highest temporal growth rate. The feedthrough factor describes how the perturbation on the unstable interface (β) "feeds through" to the stable interface (α). This feedthrough factor, for $|\omega_1 t| \gg 1$, is given by

$$\frac{\xi_{x1}(x = \alpha, t \to \infty)}{\xi_{x1}(x = \beta, t \to \infty)} = F_a(\omega_1) = F_b(\omega_1), \tag{32}$$

since for large time, the most unstable MRT mode ($\omega = \omega_1$) becomes dominant, and $F_a(\omega_1) = F_b(\omega_1)$ is simply the ratio of the ripple amplitudes between the α-interface and the β-interface for this mode [cf. Eq. (21) or (22)]. That is, $F_a(\omega_1) = F_b(\omega_1)$ gives the fraction of the disturbance on the unstable interface that is transmitted to the stable interface. In general, this feedthrough factor, Eq. (32), is exponentially small if $k\Delta \gg 1$, as it is roughly measured by $e^{-k\Delta}$.[1,8,32,33] Examples of the feedthrough factor, together with the asymptotic dependence for large and small $k\Delta$, have been given in Ref. 8 for this special case, $\rho_{01} = \rho_{03} = 0$, $h_1 = h_3 \to \infty$.

We next calculate the temporal evolution of the ripples on the α- and β-interface. We assume the following initial conditions of the ripples at the α- and β-interface at $t = 0$ (Fig. 1)

$$\xi_\alpha(0) = \xi_{\alpha0}, \tag{33a}$$

$$\xi_\beta(0) = \xi_{\beta0}, \tag{33b}$$

$$\xi'_\alpha(0) = 0, \tag{33c}$$

$$\xi'_\beta(0) = 0, \tag{33d}$$

where the prime denotes a time derivative. Thus, initially, the sinusoidal ripples (with wavenumbers k_y and k_z) at the interfaces $x = \alpha$ and $x = \beta$ have an amplitude $\xi_{\alpha0}$ and $\xi_{\beta0}$,

respectively, but with zero initial velocity. Since there are four modes, ω_1, ω_2, ω_3, and ω_4, according to the dispersion relation, Eq. (24) or (31), any surface ripple with $\exp(-ik_y y - ik_z z)$ dependence may be written as a superposition of these four modes. Specifically, we may write the ripple at the lower interface ($x = \beta$) as

$$\xi_\beta(t) = p_1 e^{i\omega_1 t} + p_2 e^{-i\omega_1 t} + p_3 e^{i\omega_3 t} + p_4 e^{-i\omega_3 t}, \quad (34)$$

where the p_i's ($i = 1, 2, 3, 4$) are constants, and we have used the result that the eigenfrequencies appear in ($\pm$) pairs, Eq. (31). The coefficients p_1, p_2, p_3, and p_4 are determined from the initial conditions. Applying Eq. (22), or Eq. (21), to each of the four modes in Eq. (34), we write the temporal evolution of the ripple on the upper interface ($x = \alpha$),

$$\begin{aligned}\xi_\alpha(t) &= p_1 F_b(\omega_1) e^{i\omega_1 t} + p_2 F_b(-\omega_1) e^{-i\omega_1 t} \\ &\quad + p_3 F_b(\omega_3) e^{i\omega_3 t} + p_4 F_b(-\omega_3) e^{-i\omega_3 t} \\ &= p_1 F(\omega_1) e^{i\omega_1 t} + p_2 F(\omega_1) e^{-i\omega_1 t} \\ &\quad + p_3 F(\omega_3) e^{i\omega_3 t} + p_4 F(\omega_3) e^{-i\omega_3 t}. \end{aligned} \quad (35)$$

In Eq. (35), we have defined $F(\omega) \equiv F_b(\omega)$ which is an even function of ω [since $F_b(\omega)$ is a function of ω^2, Eq. (22)], and have used $F(\omega_1) = F_b(\omega_1) = F_b(-\omega_1) = F_a(\omega_1) = F_a(-\omega_1)$, and $F(\omega_3) = F_b(\omega_3) = F_b(-\omega_3) = F_a(\omega_3) = F_a(-\omega_3)$. Applying Eq. (34) to Eqs. (33b) and (33d) and also applying Eq. (35) to Eqs. (33a) and (33c) yields four equations with four unknowns (p_1, p_2, p_3, and p_4), which are easily solved in terms of $\xi_{\alpha 0}$ and $\xi_{\beta 0}$. Equations (34) and (35) then read

$$\xi_\beta(t) = 2p_1 \cos(\omega_1 t) + 2p_3 \cos(\omega_3 t), \quad (36a)$$

$$\xi_\alpha(t) = 2p_1 F(\omega_1) \cos(\omega_1 t) + 2p_3 F(\omega_3) \cos(\omega_3 t), \quad (36b)$$

$$\begin{aligned}2p_1 = 2p_2 &= \frac{\xi_{\beta 0} F(\omega_3) - \xi_{\alpha 0}}{F(\omega_3) - F(\omega_1)}, \\ 2p_3 = 2p_4 &= \frac{-\xi_{\beta 0} F(\omega_1) + \xi_{\alpha 0}}{F(\omega_3) - F(\omega_1)}. \end{aligned} \quad (37)$$

It is clear that Eq. (36) satisfies the initial condition (33) and that the feedthrough factor from the β interface to the α interface is $F(\omega_1)$ for the modes $\omega = \pm\omega_1$, and is $F(\omega_3)$ for the modes $\omega = \pm\omega_3$. If the equilibrium profile is allowed to vary slowly in time, so are the eigenfrequencies $\pm\omega_1$ and $\pm\omega_3$. The factors $\cos(\omega_1 t)$ and $\cos(\omega_3 t)$ in Eq. (36) are to be replaced by $\cos(\int_0^t dt' \omega_1(t'))$ and by $\cos(\int_0^t dt' \omega_3(t'))$, respectively, according to the WKBJ approximation. Good agreement using this WKBJ technique was reported by Sinars *et al.*[7] when compared with their MRT experiments with seeded initial perturbations on the liner surface.

Equations (36) and (37) give the temporal evolution of the interface ripples for a specific, single wavenumber in k_y and in k_z, i.e., when the Fourier spectrum of the initial surface roughness on the α- and β-surface is a delta function in k_y and in k_z. In general, the initial perturbations on the α- and β-surface may be represented by their spatial Fourier transforms

$$\xi_\alpha(t = 0, k_y, k_z) = f_\alpha(k_y, k_z), \quad \xi_\beta(t = 0, k_y, k_z) = f_\beta(k_y, k_z). \quad (38)$$

The subsequent evolution of these surface perturbations on the α- and β-surface is then given by superposition (in the present linear theory)

$$\begin{aligned}\xi_\alpha(t) &= \int\int dk_y dk_z \xi_\alpha(t, k_y, k_z) e^{-ik_y y - ik_z z}, \\ \xi_\beta(t) &= \int\int dk_y dk_z \xi_\beta(t, k_y, k_z) e^{-ik_y y - ik_z z}, \end{aligned} \quad (39)$$

where $\xi_\alpha(t, k_y, k_z)$ and $\xi_\beta(t, k_y, k_z)$ are given by Eq. (36) in which $\xi_{\alpha 0}$ and $\xi_{\beta 0}$ that appear in Eq. (37) are to be replaced by $f_\alpha(k_y, k_z)$ and $f_\beta(k_y, k_z)$ respectively. For the special case where $f_\alpha(k_y, k_z)$ and $f_\beta(k_y, k_z)$ are delta functions at k_y and k_z, with amplitudes $\xi_{\alpha 0}$ and $\xi_{\beta 0}$, respectively, the general solution Eq. (39) reduces to Eq. (36). Thus, Eq. (39) gives the exact expression for the temporal evolution of surface ripples in Fig. 1, according to the linear theory, when the initial surface ripples at the α- and β-surface are characterized by the Fourier transforms, Eq. (38). If the equilibrium profile is allowed to vary slowly in time, Eq. (39) remains valid under the WKBJ approximation, in the manner discussed following Eqs. (36) and (37).

V. NUMERICAL EXAMPLES

The Cartesian, sharp boundary model presented in this paper (Fig. 1) is applied to two cases: one with $k\Delta \gg 1$ so that the feedthrough factor is negligible (case 1), and the other with $k\Delta$ of order unity, so that the feedthrough factor can be significant (case 2). In the second case, of special interest is the effect of orthogonal magnetic fields on the feedthrough factor. In both cases, we have in mind Sandia's cylindrical liner experiments,[7] and the arbitrary Lagrangian-Eulerian (ALE) radiation magnetohydrodynamics (RMHD) code HYDRA[34] to simulate them. The MHD package is not currently capable of 2D planar calculations involving orthogonal magnetic fields. A direct comparison of the HYDRA result with the complete Cartesian model in this paper is thus not possible. However, we can include the planar simulation with only a driving azimuthal ($\sim B_y$) field. Nevertheless, case 1, which corresponds essentially to Sinars' experiments,[7] provides an excellent blueprint to test our MRT calculations. This approach is then adopted for case 2.

Case 1. $k\Delta \gg 1$, negligible feedthrough: Sinars *et al.*[7] studied MRT growth on a cylindrical aluminum tube with an outer radius of 3.168 mm and inner radius of 2.876 mm (a liner thickness $\Delta = 292 \, \mu m$), driven by an axial current of order 20 MA in 150 ns. Axisymmetric sinusoidal perturbations (with azimuthal mode number m = 0) were seeded on the liner's outer surface along the axial direction with two axial wavelengths (λ_z), 400 and 200 μm, and a peak-to-valley amplitude of 5% the wavelength (20 and 10 μm). The value of $k\Delta = k_z \Delta$ equals to 4.59 and 9.17 for λ_z equal to 400 and 200 μm, respectively. The respective feedthrough factors, of order $e^{-k\Delta}$,[1,8,32,33] are 0.0102 and 0.000104; both are very small compared with unity. In such cases, the evolution of

any perturbations on the outer (inner) surface is essentially independent of any perturbation evolution on the inner (outer) surface.[8,10,11] This reduces the problem to a single-interface MRT problem, which substantially simplifies Eqs. (24)–(27). See Appendix B 3; and Ref. 8. Moreover, the factor $k_z r$ is much larger than unity, equal to 49.76 and 99.52, respectively, for λ_z equal to 400 and 200 μm, when evaluated at the outer liner radius. Thus, the planar geometry is an excellent approximation to evaluate the seeded MRT perturbation on the outer surface. If $\xi_\beta(t)$ represents the ripple amplitude on the outer liner surface (Fig. 1) and γ the fastest growing mode as determined from Eqs. (24)–(27), the surface evolution, for the $\lambda_z = 400\,\mu$m case, is governed by

$$\frac{d^2\xi_\beta(t)}{dt^2} = \gamma^2 \xi_\beta(t) = \left[k_z g(t) - \frac{(k_z B_{01z})^2 + (k_z B_{02z})^2}{\mu_0 \rho_{02}} \right] \xi_\beta(t),$$

$$\xi_\beta(0) = 20\,\mu\text{m}, \quad \dot{\xi}_\beta(0) = 0, \qquad (40)$$

where we include an axial magnetic field, B_{01z}, exterior to the liner (modeled by region I in Fig. 1) and, B_{02z}, within the liner (modeled by region II in Fig. 1). With m = 0, and $B_{01z} = B_{02z} = 0$ in Eq. (40), $\mathbf{k} \cdot \mathbf{B}_0 = 0$, and $k = k_z$, so the growth is well represented by $\sqrt{k_z g}$, which was used by Sinars et al.[7] We note that in many cases, the density and magnetic field may also be functions of time.

Next, we briefly describe the development of the HYDRA simulations. For Sinars' experiment, the liner was machined to be azimuthally symmetric (m = 0), so the simulation consisted of a seeded aluminum liner in cylindrical geometry (r,z) over a 1.2 mm axial extent, including two wavelengths each of the 400 and 200 μm sinusoidal perturbations. The mesh was conformed to the sinusoidal perturbations, but did not include the 100 nm rms machining roughness from experiment. The axial zoning maintained greater than 30 zones/200 μm wavelength, and ratioed zoning within the liner kept the radial resolution at ~1 μm. The simulations were driven using the load current from z1965 (roughly 20 MA in 150 ns) as determined from the load current in Sinars et al.[7] We are particularly interested in applying our model to realistic scenarios, so we made use of SESAME EOS table 3719,[42] and Quotidian- Lee-More-Desjarlais[43] (QLMD) electrical conductivities for aluminum. However, we neglect radiation physics since this does not

play a significant role in these experiments. Later, we also consider a case where the liner resistivity is small and constant to mimic ideal MHD.

The 2D HYDRA simulations had to be distilled into MRT amplitude data, which can be done in a number of ways. First, the mass per unit length, $m_L(z)$, could be computed for each axial height and then a Fast Fourier Transform (FFT) could be taken of $m_L(z)$ at each simulation time. With a large enough axial extent and resolution the amplitude of the FFT at 400 or 200 μm would then give the MRT growth at that amplitude as a function of time. Due to the limited axial extent of the simulation, this method was not sufficiently accurate, as the amplitude was consistently underestimated. The method settled on to determine the MRT growth was to calculate the bubble and spike radii directly from the simulation data. However, for a better comparison with the experimental data, we post-process the 2D data using the spectral analysis code, SPECT3D[44] to generate simulated radiographs, with a 6.151 keV back-lighter with 15 μm resolution, angled 3° off axis.[45] The setup is similar to Figure 2 from Sinars et al.[7] From this new 2D data, in lieu of an FFT, we chose a transmission contour and located the radial position of this contour at each axial position. The range of transmission contours showed an excellent representation of the bubble and spike radii, the difference of which being the MRT amplitude. Overall, the images were quite clean and the variation in the transmission contours was small. The 50% contour was roughly the average position so the 2D HYDRA data in Fig. 2 were obtained using this contour.

We next consider a general technique to determine the input parameters for our analytic model. For the 3-region problem shown in Fig. 1, the instantaneous quantities assumed in each region, $\mathbf{B}_{01}$, $\mathbf{B}_{02}$, $\mathbf{B}_{03}$, ρ_{01}, ρ_{02}, ρ_{03}, and the remaining parameters, g, Δ, h_1, and h_3, are most easily extracted from the 1D HYDRA data to compute $\xi_\beta(t)$ and $\xi_\alpha(t)$. A single 1D HYDRA run is fast and gives the general liner dynamics required for our model and can be used for any wavenumber. The goal is to determine from each simulation timestep, the corresponding instantaneous eigenmodes and feedthrough factors. The most general way to accomplish this using our linear model would be to directly integrate Eq. (16) using the radial profile from HYDRA, but this
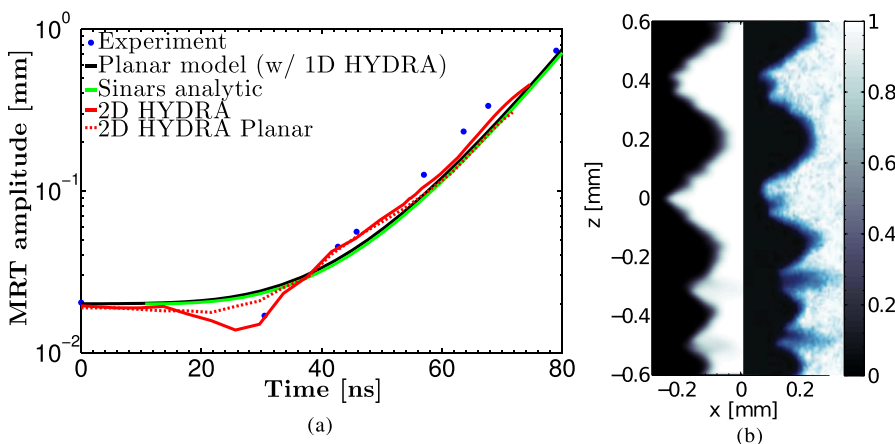

FIG. 2. (a) Comparison of Sinars' experiment and analytic model,[7] 2D HYDRA simulation (planar and cylindrical), and our analytic planar model (Eq. (40)), for the seeded $\lambda_z = 400\,\mu$m perturbation. (b) An example simulated radiograph (left) is compared to an experimental radiograph[7] (right) at $t = 63.5$ ns.

can be unduly challenging due to the noisy spatial derivatives in the hydro data. Thus, our spatially uniform input parameters come from calculating average quantities from each HYDRA timestep. Before continuing, we acknowledge a particular challenge of using the sharp boundary model for a diffuse liner is how to define the boundary itself.

For example, we consider how to compute ρ_{02}, which corresponds to the liner density. The bounds on the liner from HYDRA are the Lagrangian nodes separating the liner from vacuum, which also gives the maximum radial extent of the liner (the thickness, Δ). This can be an overestimate of the thickness depending on how diffuse the liner material becomes or if there is significant ablation. Hence, the overall thickness may change over time as well as the average density. With these bounds, we can simply radially average over the liner thickness: $\rho_{02} = \int_{r_\alpha}^{r_\beta} r\rho(r)dr / \int_{r_\alpha}^{r_\beta} rdr$. A similar process can be performed for the other input parameters. B_{y1} (the drive field) is taken to be the maximum value in the vacuum otherwise it is severely underestimated by the above averaging. The effective $g(t)$ can also be computed from our equilibrium condition, Eq. (7), though in this instance, it is not much different from the calculation in Sinars *et al.*, as shown in Fig. 2. With these averaged parameters, γ is computed and we continue to the next timestep.

Figure 2(a) shows a comparison of our complete set of calculations along with Sinars' data. First, we note excellent agreement is observed between experiment, 2D simulations, and our analytic planar model (using 1D HYDRA runs as input as described above) indicating linear MRT growth in the absence of feedthrough even as the amplitude of perturbation growth exceeds twice the wavelength of the perturbation. Second, good agreement is observed between the Cartesian (x,z) and cylindrical (r,z) HYDRA simulations which gives us good confidence in the applicability of our planar model to the developing MRT, at least for the majority of plotted times since the convergence is low. In future work, we plan to examine to what radius this agreement can be maintained. Additionally, in Fig. 2(b) we provide a comparison of synthetic (produced from 2D HYDRA data in cylindrical geometry) and experimental[7] radiographs at 63.5 ns. This shows that HYDRA qualitatively reproduces a similar mode structure as observed in Sinars' experiment.

We next consider adding an axial seed magnetic field for liner implosions on the Z-machine. The current state of the art technology can apply up to 10 T (B_z). From both our analytic and 2D HYDRA simulations, this field was found to be insufficient to mitigate the exterior MRT growth for 400 μm, so we consider a 100 T case in our simulation. For our planar analytic model, the axial field is initially uniform throughout the problem domain ($B_{01z} = B_{02z} = B_{03z} = B_{0z}$), and then allowed to evolve according to 1D HYDRA simulations. The exterior field (B_{01z}) remains roughly its initial value throughout the duration of the implosion, while the field within the liner itself (B_{02z}) and inner vacuum region are compressed (B_{03z}). For both a 10 and 100 T case, the axial magnetic field has little effect on the implosion dynamics unless the axial field is strongly compressed, which is not the case for the time range shown.

At 100 T, the stabilization term from the magnetic field line bending $\sim (k_z B_z)^2 / \mu_0 \rho_0$ remains larger than the destabilizing MRT term $k_z g$ for a much longer period of time, while the drive field ramps up, hence the delayed growth, as seen in Fig. 3(a). Equation (41) illustrates this, given that the liner is fairly thick ($k\Delta > 1$), the single interface MRT growth rate, γ, is

$$\gamma^2 = \frac{(\rho_{liner} - \rho_{vac})}{\rho_{liner} + \rho_{vac}} kg - \frac{(k \cdot B_{z,liner})^2 + (k \cdot B_{z,vac})^2}{\mu_0 (\rho_{liner} + \rho_{vac})} \quad (41)$$

$$\approx kg - \frac{(k \cdot B_{z,liner})^2 + (k \cdot B_{z,vac})^2}{\mu_0 \rho_{liner}}. \quad (42)$$

However, the presence of a 100 T seed field in simulation does not show the same level of instability reduction predicted by the analytic model, which is presented in Fig. 3(a). Partially responsible for this discrepancy is that while the current is increasing, the liner exterior is heating and ablating material just as with the 0 T case. Close inspection of the 2D HYDRA simulations shows that the magnetic field bending is concentrated in the liner, so while there is $B_{z1} > 0$ in the vacuum region, $k \cdot B_{z1} = k \cdot B_{z,vac} \approx 0$, which effectively reduces the stabilization by $1/2$ (Eq. (42)). Though the field lines remain somewhat frozen into the liner, the field lines easily diffuse in the highly resistive vacuum in HYDRA.
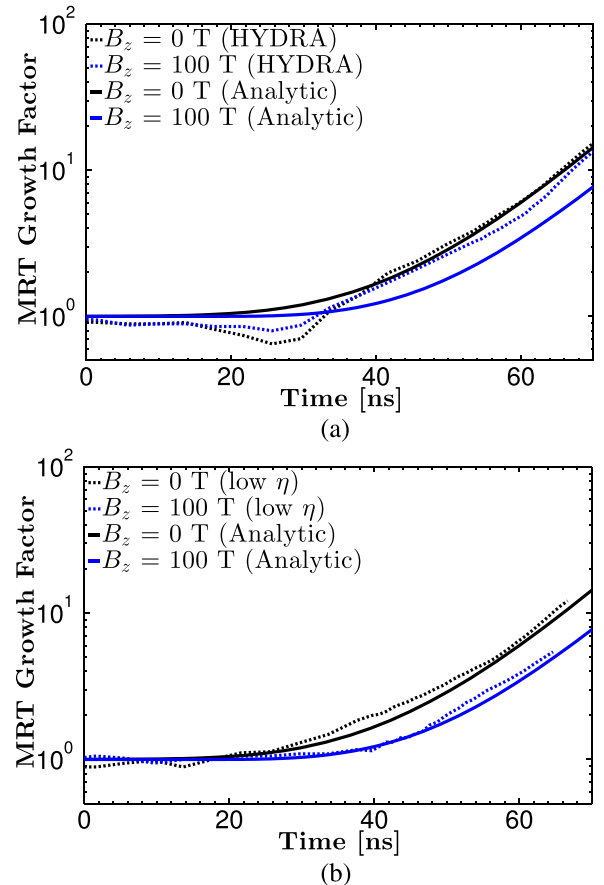

(a)

(b)

FIG. 3. MRT growth factors, solid curves are analytic model with 1D HYDRA input, dashed curves are 2D HYDRA simulations, with given applied axial field, for 400 μm perturbation (a) QLMD resistivity simulations, (b) ~ideal MHD simulations.

Additional 2D simulations were run to obtain results for an ideal MHD plasma. This was accomplished by setting the liner resistivity, η, to be constant and small. For the sake of the diffusion solver, the resistivity could not be set arbitrarily small, but set to minimize the diffusion of the field into the liner over only a handful of zones. The results of two such simulations (0 T and 100 T) are shown in Fig. 3(b) as the low η (highly conductive) case for direct comparison with Fig. 3(a). Here, the 100 T growth is much closer to what is expected from our analytic calculation. With the field lines better frozen into the liner, for the low resistivity case, the magnetic tension is greater and provides the anticipated stabilization. Techniques similar to those used by Zhang[12] could be used to analyze the effect of a magnetic field distribution, both axial and azimuthal, in more detail. However, it is possible that inclusion of an axial field in realistic situations might invalidate our ideal MHD assumption and care must be taken when determining stabilization due to field line bending.

Case 2. $k\Delta$ of order 1, moderate feedthrough: We now consider two examples, both illustrating cases where feedthrough is significant: (a) an idealized liner focusing on the impact of a stabilizing axial field on long wavelength feedthrough and (b) HYDRA verification of feedthrough for various wavelengths. Originally, we intended to also calculate feedthrough growth for Sinars' data from case 1. Although the feedthrough factor itself was expected to be quite small (on the order of 1% for 400 μm) after about 60 ns, the product of $F(\omega)\,\xi_{\mathrm{MRT}} \approx 1\,\mu$m which could still be compared to our planar theory. This analysis brought an important caveat of our model to our attention. That is, the presence of a shock developing in the liner can severely impact feedthrough, depending upon the wavelength. The two main problems were (1) seeding of the inner surface by a rippled shock impact and (2) strong growth of the Richtmyer-Meshkov instability after the shock.[33] As such we leave the detailed analysis of shocks to a future publication. Here in example (a), we ignore this shock and consider only the effect of a large stabilizing axial field in our planar analytic model. In example (b), we utilize a quasi-isentropic current pulse to minimize the shock and also consider larger wavelengths, which have larger feedthrough factors.

Example (a): We set $\lambda_z = 1.5$ mm and $\Delta = 292\,\mu$m, the same liner thickness as in case 1 above. We again set $k_y = 0$ (i.e., m = 0). In this case, $k\Delta = k_z\Delta = 1.223$ and the feedthrough factor, $e^{-k\Delta} = 0.294$, which may be considered as rather significant. Alternatively, we could have also reduced the liner thickness to achieve the same feedthrough factor for a shorter wavelength. First, we provide a nominal case without an applied axial field, where we expect uninhibited feedthrough of the outer to inner surface and then a case including an axial field. To use the planar slab geometry (Fig. 1) to assess the effects of a compressed axial magnetic field on the feedthrough, we assume that $h_1 \to \infty$, $\rho_{10} = 0$, and B_{01z} may be time dependent, that is, the region exterior to the liner (region I) is unbounded, it has a very low mass density, and assumes the initial seed of 10 T axial magnetic field throughout. The magnetic drive is given by $B_{01y} = B_{0\theta}(t)$, which is the same as used in case 1. For the

liner (region II), we assume that $\Delta = 292\,\mu$m, ρ_{20} and B_{02z} are time dependent and $B_{02y} = 0$, that is, the liner (region II) maintains a constant thickness, while the density and magnetic field may compress if present, and zero azimuthal magnetic field. The benefit of assuming constant thickness effectively removes the dependence on thickness and focuses on changes only due to the Alfven terms, which may evolve with time. Thus, we analyze incompressible MRT perturbations of a liner that has undergone compression. For the center region (region III), we assume that $h_3 \to \infty$, $\rho_{03} = 0$, $B_{03y} = 0$, and B_{03z} may be time dependent; that is, the region inside the liner (region III) is unbounded, it also has a very low mass density, has the axial magnetic field $B_{03z}(t)$ being compressed according to the 1D HYDRA model if present, and a zero azimuthal magnetic field B_{03y}.

Plotted in Fig. 4(a) are the normalized growth factors, in amplitude, from Eqs. (36) and (37) assuming there is no initial perturbation on the inner surface ($\xi_{z0} = 0$) and we have converted the absolute time scale to the increase of the axial
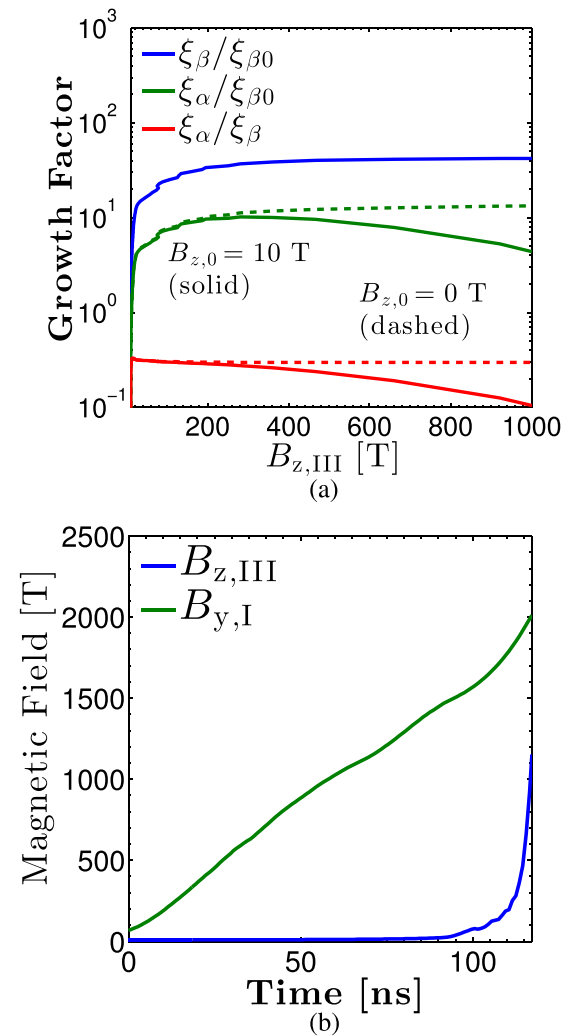

FIG. 4. (a) Evolution of the outer surface, ξ_β, and the initially unperturbed "inner" surface, ξ_α, as a function of the compressing axial field for a 1.5 mm wavelength perturbation. The initial seeded axial magnetic field is 10 T (solid) and the 0 T case (dashed) is included at the equivalent time for each value of B_z as determined from (b). (b) Evolution of the drive and axial magnetic field (in region III) as a function of time.

field. The dashed lines are plotted at the equivalent time, determined from 1D HYDRA, from Fig. 4(b) since $B_z = 0$. For example, if we look at $B_{z,\text{III}} = 800\,\text{T}$ along the x-axis of Fig. 4(a), this corresponds to very late in time if we look at Fig. 4(b). This essentially means that we have parameterized the zero field case as a function of the axial field of the seeded case, since we have a mapping from time to axial magnetic field. This is done to highlight the damping apparent in Fig. 4(a) once $B_z \approx 500\,\text{T}$ which is a significant fraction of B_y from Fig. 4(b) at that time. The story told by Figure 4(a) is then that damping of the inner surface ripple (ξ_α) occurs only once the B_{03z} field strength is comparable to the drive field. Generally, this requires significant compression of the seed field.[8,12] It should be noted that while this damping is occurring, g remains positive which means the deceleration phase has not yet begun.

Figure 4 shows the growth of the inner surface over many e-foldings. Important to keep in mind is that while the MRT growth stays surprisingly linear for some 70 ns, for later times, this growth becomes nonlinear and feedthrough is more difficult to interpret as the bubble and spike structure becomes more pronounced. Comparisons of our planar analytic model and 2D HYDRA simulations for various wavelengths are presented in example (b).

We can perform a similar calculation, without the axial field, where the inner surface is seeded with the same perturbation as the outer surface, $\xi_{\alpha 0} = \pm \xi_{\beta 0}$, with both in and out of phase scenarios (Fig. 5). With the perturbations in phase, the overall feedthrough is less than with the un-seeded inner surface, whereas the out of phase seeding has larger feedthrough than the un-seeded case. Due to the presence of four modes, beating occurs on the ripples on the two surfaces [Eqs. (34) and (35)]. The beating among the linear modes before the most unstable mode dominates also occurs analogously near the input of a traveling wave tube (TWT). It gives rise to the "launching loss" during the spatial amplification on a TWT.[46] This effect is quantified in Fig. 5 where we focus on the inner surface feedthrough alone.

Example (b): A realistic 2D simulation of a typical liner, without machined perturbations, would start with quasi-random surface roughness. With this type of surface,
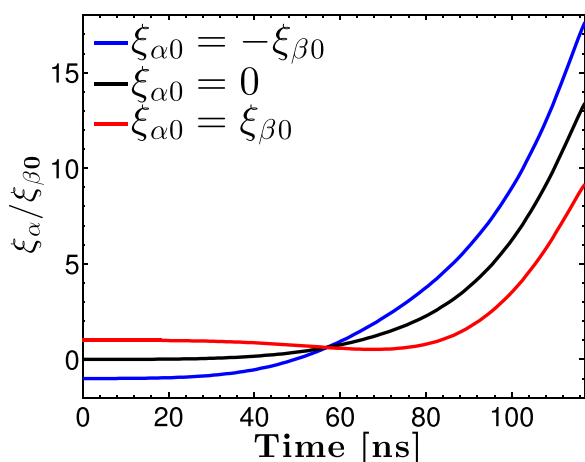
feedthrough becomes important in the later stages of MRT growth after short wavelength modes from the surface seeding have cascaded and collected into longer wavelengths, which have a corresponding larger feedthrough factor. Besides increasing the liner thickness, as shown in example (a) an axial field comparable to the drive is another way to mitigate feedthrough.[8] In pre-magnetized cylindrical implosions, this situation generally occurs late in a typical current pulse. This requires substantial resolution to model the surface roughness through high compression. Such high-resolution simulations can also artificially enhance growth rates due to the enforced perfect correlation of short wavelength modes.[47] So we study a more ideal case, using various seeded wavelengths, and use an artificially large axial field to avoid large compression to study feedthrough in a more controlled manner. The last requirement was mitigation of shock formation, which was done by modifying the drive current.

A quasi-isentropic current pulse was derived from the work of Martin *et al.*[48] by adding a moderate foot to lengthen the pulse in time and reducing the peak current. 1D HYDRA simulations were run, modifying the current as needed to reduce the development of a shock. The result is the current pulse shown in Fig. 6(a), which minimizes shock formation until later in time. However, even with a perfectly designed isentropic compression pulse, a finite delay time exists due to the finite sound speed of the material. Figure 6(b) shows the corresponding normalized inner surface growth for the same liner as in case 1, but with four different wavelength perturbations (200, 400, 800, and 1500 μm). The solid lines

FIG. 5. Evolution of the inner surface $\xi_\alpha(t)$ for $\lambda = 1.5$ mm with three initial seedings (top to bottom): out of phase, no seed, and in phase.
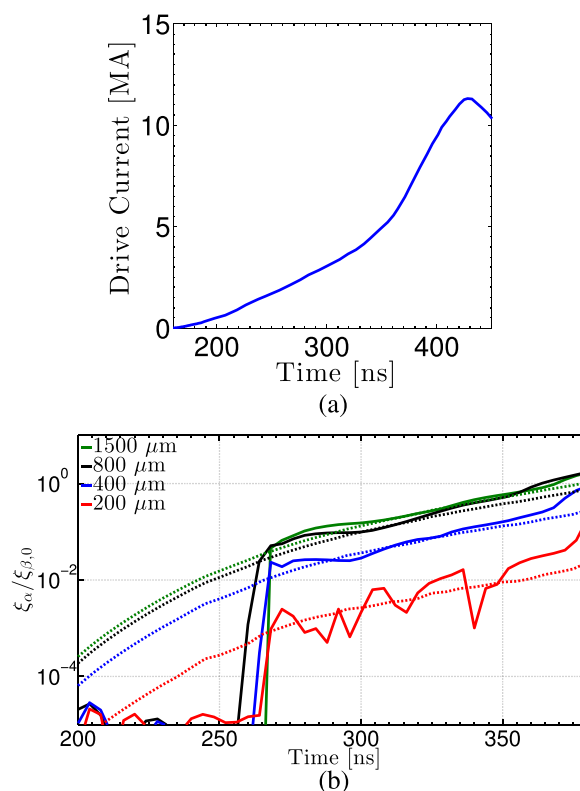

FIG. 6. (a) Current pulse reducing shock strength that drives the simulations in (b). (b) Comparison of 2D HYDRA simulations and analytic calculations of the inner surface feedthrough for four different wavelength perturbations.

come from 2D HYDRA simulations and the dashed are the analytic planar calculations. Before 260 ns, the inner surface remains roughly at the grid resolution noise level, but at 260 ns a weak shock arrives bringing the surface perturbation amplitude to the expected level of feedthrough. The following growth is evidently not dominated by Richtmyer-Meshkov instability as the scaling is not linear in time but exponential, in accordance with feedthrough. At 360 ns, this is not the case, as there is a fast uptick in growth corresponding to large increase in the dI/dt of the pulse.

Despite this, the agreement with feedthrough scaling is quite good for a significant portion of the pulse. The characteristic wavelength dependence is clearly observed, as the liner thickness is the same for all three simulations.

We next study the effect of an axial field. To avoid the high convergence required to compress a 10 T seed field (and subsequent departure from planar geometry), we initialize 2D HYDRA simulations with a 100 and 200 T field, which keeps the axial field on the order of the drive field for the majority of the pulse. Figure 7 shows the reduction of inner surface growth via 2D HYDRA simulations for an 800 μm perturbation when a sufficiently strong axial field is present by taking the ratio of the inner surface amplitude with the field to without the field. This in effect plots the ratio of the instantaneous feedthrough factors: F_{B_z}/F_0 as defined by Eq. (22) for the dominant growing mode. Values less than one indicate feedthrough reduction, while early time ratios greater than one correspond to the arrival of a magnetic diffusion wave from liner compression. As the plasma is compressed, the field lines are bent which also bends the plasma corresponding to slightly earlier feedthrough.

Comparison with analytic theory when including an axial field is again made difficult due to resistive effects. For 200 T, our planar theory would predict nearly zero feedthrough and once again the ideal MHD simulation shown in Fig. 7, as the dashed curve, agrees best showing almost an order of magnitude smaller feedthrough with the field. Case 1 showed that in the exterior vacuum region $\mathbf{k} \cdot \mathbf{B}_{z1} = \mathbf{k} \cdot \mathbf{B}_{z,vac} = 0$ otherwise MRT reduction is quite overestimated. However, if we assume this to be true in region III as well, the feedthrough factor is then independent of the axial field ($e^{-k\Delta}$), which we have just shown in Figure 7 as not true. Even if we again set $\mathbf{k} \cdot \mathbf{B}_{z1} = 0$ and keep $\mathbf{k} \cdot \mathbf{B}_{z3} > 0$, the feedthrough calculation using Eqs. (35)–(37) still

overestimates the growth reduction. Overall, we observe over 50% (25%) reduction in inner surface growth including the 200 T (100 T) field from simulations. This reduction does in fact fall with the range predicted by the planar model if we consider only the ratio F_{B_z}/F_0 whose values span from 0.25 to 0.55, which strongly depend on the thickness as well as g over this timescale.

Thus, our analytic model does indeed provide some insight into feedthrough and its reduction by an axial field, but detailed quantitative comparison is still challenging. We have merely provided one example with one wavelength and two axial field values to show the possibility of feedthrough reduction. Larger feedthrough reduction was observed with a 400 μm perturbation and we expect less feedthrough reduction for larger wavelengths. Additional simulations are underway to scan the full mode space and required fields for subsequent feedthrough reduction.

In this section, we have applied our planar model to similar conditions that would occur in a very weakly shock compressed liner implosion and determined the inner and outer surface evolutions for a number of different initial perturbations. An example of feedthrough reduction using an axial field was presented and opens the door for further investigation into this effect for various initial conditions (axial fields and perturbation spectrum). The effect of a convergent geometry on these results will be examined in a future publication.

We should stress that Eqs. (36) and (37) are equally valid in cylindrical geometry, one needs only determine the new eigenvalues and corresponding feedthrough factors. The most important feature in the cylindrical geometry is the coupling between the MRT mode and the kink (m = 1) and sausage (m = 0) mode. The kink and sausage instabilities are absent in the Cartesian model,[8,37] but are the dominant instability in cylindrical geometry when g = 0. Nonetheless, we have illustrated the application of our theory to some practical situations, which could be of particular use in other magnetically accelerated systems[13,14,22–25] besides liner implosions or Z-pinches.

VI. CONCLUDING REMARKS

The sharp boundary model given in this paper provides a quantitative evaluation of the temporal evolution of arbitrary initial perturbations on the interfaces of a finite plasma slab that is subjected to MRT. The plasma slab is bounded by rigid, perfect conductors so that magnetic compression may be modeled. By allowing the equilibrium to evolve, the instantaneous growth rate may be explicitly calculated in a WKBJ analysis, as given in Eq. (39) and explained in the discussions that follow. In the examples, we adopted such a WKBJ analysis to Sinars' experiments on MRT growth that resulted from some seeded initial perturbations on the cylindrical liner.[7] We used the data from 1D HYDRA simulation to construct the evolving parameters in the equilibrium profiles that need to be specified in the slab model. The consistent results obtained encouraged us to use a similar approach to assess the effects of a compressed axial magnetic field on the feedthrough in the liner. Our analytic results show that the compressed axial magnetic field would have a significant
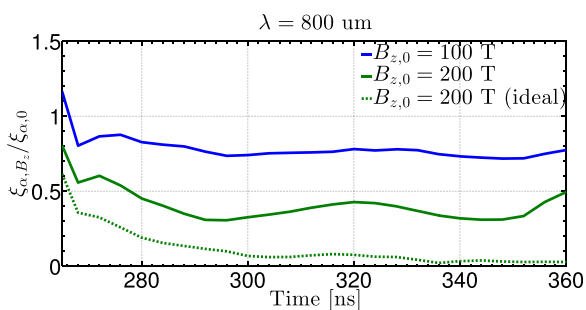
FIG. 7. Ratio of the inner liner surface amplitude with a 100 and 200 T axial field to that of one without the axial field showing feedthrough reduction for the majority of the times of interest. The dashed line shows the 200 T case using an ~ideal MHD approach as in case 1.

effect on feedthrough only when it is comparable to the driving (azimuthal) magnetic field.[8,12] Evidence for feedthrough reduction via a strong axial field was shown in 2D simulations. We also found that the feedthrough depends on the relative phase of the initially seeded perturbations on the two surfaces of the liner. Overall, our model agrees well with MRT growth from simulation even when the liner is shock compressed while analysis of feedthrough in this situation may require additional considerations for long wavelengths. While the temporal evolution of general 3-D initial perturbations can be calculated explicitly using Eq. (39), 3-D simulations of similar initial conditions are at the edge of numerical code capability. Equations (36) and (37) is well suited to describing the evolution of a single well-defined mode. Additional challenges appear when one considers how the electrothermal instability[39–41] could develop a spectrum of growing modes which could interact and somehow give way to much larger wavelength MRT growth that is observed later on in these implosions.

The most serious deficiency inherent in the planar slab model, for cylindrical implosions such as MagLIF, is that it cannot account for the kink and sausage mode in a cylindrical plasma column (or cylindrical liner).[8] This can be proven from Eq. (16), which shows that ω^2 is always real and positive if $g = 0$, regardless of the equilibrium mass density or current density profiles.[3,37,49] For an imploding cylindrical liner, the kink mode, the sausage mode, and the MRT mode may all be tightly coupled. The true nature of this coupling is largely unknown because they are all driven unstable by the same axial current. We are currently studying the coupling between the kink, sausage, and MRT mode using a cylindrical geometry. Additionally, in the present model, the feedthrough from the β-surface to the α-surface (Fig. 1) occurs instantaneously because the assumption of incompressibility implies an infinite sound speed. In many implosion experiments, a shock is initiated from the outer surface and the feedthrough to the inner surface would not occur until the shock's arrival. The analysis of shock-induced feedthrough, using both HYDRA simulations and analytical modeling, will be presented elsewhere.

ACKNOWLEDGMENTS

APPENDIX A: ALTERNATE DERIVATION OF THE DISPERSION RELATION AND THE FEEDTHROUGH FACTOR

In this Appendix, we outline the alternate derivation of the dispersion relation, Eq. (24). A key step is to express all important quantities in terms of the fluid displacement in the x-direction, ξ_{1x}, within each region, I, II, or III (Fig. 1). Within each region, we assume that the density ρ_0 and magnetic field $\mathbf{B}_0$ is constant and uniform, and we shall drop the designation of the individual region. The perturbation quantities are given in the form of Eq. (15). We follow Chandrasekhar[3] and the systematic treatment by Melcher.[38] We state the general results obtained from the linearized ideal MHD equations.

In each region of Fig. 1, all perturbation quantities may be expressed in terms of ξ_{1x}. First

$$\xi_{1y} = \frac{k_y}{ik^2}\frac{\partial \xi_{1x}}{\partial x}, \tag{A1}$$

$$\xi_{1z} = \frac{k_z}{ik^2}\frac{\partial \xi_{1x}}{\partial x}, \tag{A2}$$

which give all other components of the perturbation displacement in terms of ξ_{1x}. Note that the incompressibility condition, $\nabla \cdot \boldsymbol{\xi}_1 = 0$, is satisfied. The perturbation magnetic field is tied to the perturbation displacement of a perfectly conducting fluid, yielding

$$\mathbf{B}_1 = -i(\mathbf{k} \cdot \mathbf{B}_0)\boldsymbol{\xi}_1, \tag{A3}$$

which may be expressed in terms of ξ_{1x} by virtue of Eqs. (A1) and (A2). Equation (A3) gives the perturbed magnetic pressure in terms of ξ_{1x},

$$p_{m1}(x) = \frac{\mathbf{B}_0 \cdot \mathbf{B}_1}{\mu_0} = -\frac{(\mathbf{k} \cdot \mathbf{B}_0)^2}{\mu_0 k^2}\frac{\partial \xi_{1x}}{\partial x}. \tag{A4}$$

In terms of ξ_{1x}, the perturbed kinetic pressure reads

$$p_1(x) = \rho_0 \frac{\omega^2}{k^2}\frac{\partial \xi_{1x}}{\partial x}. \tag{A5}$$

There is an additional pressure due to the change in the gravitational energy that results from ξ_{1x},

$$p_{g1}(x) = -\rho_0 g \xi_{1x}. \tag{A6}$$

The total perturbation pressure, within each region, is

$$P_1(x) = p_{m1}(x) + p_1(x) + p_{g1}(x), \tag{A7}$$

which is in terms of ξ_{1x} using Eqs. (A4)–(A6). Since the total perturbation pressure is continuous across the α- and β-interface, we have

$$P_1(\alpha^+) = P_1(\alpha^-), \tag{A8}$$

$$P_1(\beta^+) = P_1(\beta^-). \tag{A9}$$

Applying the solutions of ξ_{1x} [Eqs. (19b) and (19c)] to Eq. (A8), we obtain a relation between ξ_α and ξ_β and this relation is identical to Eq. (21). Applying the solutions of ξ_{1x} [Eqs. (19a) and (19b)] to Eq. (A9), we obtain another relation between ξ_α and ξ_β and this relation is identical to Eq. (22). The dispersion relation, Eq. (23) or (24) of the text, follows.

APPENDIX B: SOME LIMITING CASES

In this Appendix, we list the values of *A*, *B*, and *C* in dispersion relation (24) for several cases of common interest. In so doing, we also illustrate how the various interesting limits

(e.g., $\rho_{01}/\rho_{02} \rightarrow 0$ or ∞; Δ, h_1, $h_3 \rightarrow 0$ or ∞) are properly taken. Once A, B, and C are known, the eigenfrequencies $\pm\omega_1$ and $\pm\omega_3$ are given by Eq. (28), the feedthrough factors for the corresponding eigenmodes are given by Eq. (21) or (22), and the temporal evolutions of the initial surface ripples are given by Eq. (36), for the fixed value of k_y and k_z.

The limiting cases include (a) the familiar deep and shallow water waves,[3,38] (b) the classical Rayleigh-Taylor instabilities,[3,32,38] (c) the single-interface MRT theory of Chandrashekhar,[3] and Kruskal and Schwartzchild,[2] (d) Harris' MRT theory for a finite slab,[1,8] and (e) some geometries relevant to flyer-plates experiments.[22,23] These limits correspond to the various limits of Fig. 1, by changing the value (or sign) of g, $\mathbf{B}_{01}$, $\mathbf{B}_{02}$, $\mathbf{B}_{03}$, ρ_{01}, ρ_{02}, ρ_{03}, Δ, h_1, and h_3.

1. Water wave

Referring to Fig. 1, water wave limit may be recovered when $\mathbf{B}_{01} = \mathbf{B}_{02} = \mathbf{B}_{03} = 0$, $\rho_{03} = 0$, $\rho_{01}/\rho_{02} = 1$. Thus, from Eqs. (25)–(27), we have

$$A = 1 + \coth kh_1 \coth k\Delta, \tag{B1}$$

$$B = kg(\coth kh_1 + \coth k\Delta), \tag{B2}$$

$$C = 0, \tag{B3}$$

which are substituted in Eq. (24) to obtain[3,38]

$$\omega^2 = kg \tanh(k(h_1 + \Delta)), \tag{B4a}$$

which is the shallow water wave with the water depth of $h_1 + \Delta$.

If $h_1 + \Delta \rightarrow \infty$, we have

$$\omega^2 = kg, \tag{B4b}$$

which is the familiar deep water wave limit.

Alternatively, we may let $\mathbf{B}_{01} = \mathbf{B}_{02} = \mathbf{B}_{03} = 0$, $\rho_{02} = \rho_{03} \rightarrow 0$. Thus, $\rho_{03}/\rho_{02} = 1$, and $\rho_{01}/\rho_{02} \rightarrow \infty$. From Eqs. (25)–(27), we have

$$A = 1 + \frac{\rho_{01}}{\rho_{02}} \coth kh_1 \coth kh_3$$
$$\quad + \left(\frac{\rho_{01}}{\rho_{02}} \coth kh_1 + \coth kh_3\right) \coth k\Delta$$
$$\cong \frac{\rho_{01}}{\rho_{02}} \coth kh_1 (\coth kh_3 + \coth k\Delta), \tag{B5}$$

$$B = kg\left(\frac{\rho_{01}}{\rho_{02}} - 1\right)(\coth k\Delta + \coth kh_3)$$
$$\cong kg\frac{\rho_{01}}{\rho_{02}}(\coth k\Delta + \coth kh_3), \tag{B6}$$

$$C = 0. \tag{B7}$$

Substituting Eqs. (B5)–(B7) into Eq. (24), we obtain[3,38]

$$\omega^2 = kg \tanh kh_1, \tag{B8}$$

which is the shallow water wave with the water depth of h_1.

If $h_1 \rightarrow \infty$, we have

$$\omega^2 = kg, \tag{B9}$$

which is the familiar deep water wave limit.

2. Classical Rayleigh-Taylor instabilities

Instead of simply changing the sign of g in Eqs. (B8) and (B9) to obtain the classical Rayleigh-Taylor instability, we refer to Fig. 1, and set $\mathbf{B}_{01} = \mathbf{B}_{02} = \mathbf{B}_{03} = 0$, $\rho_{01} = 0$, $\rho_{02} = \rho_{03}$, and $\Delta \rightarrow \infty$ (or $h_3 \rightarrow \infty$). Thus, from Eqs. (25)–(27), we have

$$A = 1 + \coth kh_3 \coth k\Delta, \tag{B10}$$

$$B = -kg(\coth kh_3 + \coth k\Delta), \tag{B11}$$

$$C = 0, \tag{B12}$$

which are substituted in Eq. (24) to get

$$\omega^2 = -kg \tanh(k(h_3 + \Delta)), \tag{B13}$$

which gives the classical Rayleigh-Taylor instability[3,32,38] with a growth rate of $\sqrt{kg}$ in the limit $\Delta \rightarrow \infty$, or $h_3 \rightarrow \infty$.

Alternatively, we may let $\mathbf{B}_{01} = \mathbf{B}_{02} = \mathbf{B}_{03} = 0$, $h_3 \rightarrow \infty$, $\rho_{01} = \rho_{02} \rightarrow 0$. Thus, $\rho_{01}/\rho_{02} = 1$, and $\rho_{03}/\rho_{02} \rightarrow \infty$. From Eqs. (25)–(27), we have

$$A = 1 + \frac{\rho_{03}}{\rho_{02}} \coth kh_1 + \left(\coth kh_1 + \frac{\rho_{03}}{\rho_{02}}\right) \coth k\Delta$$
$$\cong \frac{\rho_{03}}{\rho_{02}}(\coth kh_1 + \coth k\Delta), \tag{B14}$$

$$B = -kg\left(\frac{\rho_{03}}{\rho_{02}} - 1\right)(\coth kh_1 + \coth k\Delta)$$
$$\cong -kg\frac{\rho_{03}}{\rho_{02}}(\coth kh_1 + \coth k\Delta), \tag{B15}$$

$$C = 0, \tag{B16}$$

which are substituted in Eq. (24) to get

$$\omega^2 = -kg, \tag{B17}$$

which is the classical Rayleigh-Taylor instability[32] with a growth rate of $\sqrt{kg}$.

3. Single-surface MRT

In the single interface MRT problem considered by Chandrashekhar,[3] Kruskal and Schwartzchild,[2] the upper half space could be magnetic field-free, whereas the lower half space is vacuum filled with a magnetic field. Thus, in Fig. 1 we set $\mathbf{B}_{02} = \mathbf{B}_{03} = 0$, $\rho_{01} = \rho_{03} = 0$, $h_1 \rightarrow \infty$, and $\Delta \rightarrow \infty$, Eqs. (25)–(27) then give

$$A = 1, \tag{B18}$$

$$B = \frac{\rho_{01}}{\rho_{02}}(\mathbf{k} \cdot \mathbf{V}_{A1})^2 \coth k\Delta \coth kh_1 = \frac{(\mathbf{k} \cdot \mathbf{B}_{01})^2}{\rho_{02}\mu_0}, \tag{B19}$$

$$C = -(kg)^2 + kg\frac{\rho_{01}}{\rho_{02}}(\mathbf{k}\cdot\mathbf{V}_{A1})^2\coth kh_1$$

$$= -(kg)^2 + kg\frac{(\mathbf{k}\cdot\mathbf{B}_{01})^2}{\rho_{02}\mu_0}, \tag{B20}$$

which are substituted in Eq. (24) to get

$$\omega^2 = -kg + \frac{(\mathbf{k}\cdot\mathbf{B}_{01})^2}{\rho_{02}\mu_0}, \tag{B21}$$

which is the single interface problem considered by Chandrashekhar,[3] Kruskal and Schwartzchild.[2]

4. Harris' 2-interface slab model

Referring to Fig. 1, for the 2-interface slab problem considered by Harris,[1] the weight in region 2 is supported solely by the vacuum magnetic field $\mathbf{B}_{01}$ in region 1. As in Harris, we set $\mathbf{B}_{02} = \mathbf{B}_{03} = 0$, $\rho_{01} = \rho_{03} = 0$, $h_1 \to \infty$, and $h_3 \to \infty$. Equations (25)–(27) then yield

$$A = 1, \tag{B22}$$

$$B = \frac{(\mathbf{k}\cdot\mathbf{B}_{01})^2}{\rho_{02}\mu_0}\coth k\Delta, \tag{B23}$$

$$C = -(kg)^2 + kg\frac{(\mathbf{k}\cdot\mathbf{B}_{01})^2}{\rho_{02}\mu_0}, \tag{B24}$$

which recovers the Harris' 2-interface MRT problem.[1,8] Note $\rho_{0i}(\mathbf{k}\cdot\mathbf{V}_{Ai})^2 = (\mathbf{k}\cdot\mathbf{B}_{0i})^2/\mu_0$ has been used in deriving Eqs. (B23) and (B24) when $\rho_{0i}\to 0$.

5. MRT on flyer plates

To mimic the MRT flyer-plates geometries[22,23] in which Δ, h_1, and h_3 may all be finite, we set $\rho_{01} = \rho_{03} = 0$, and $\mathbf{B}_{02} = 0$ in Fig. 1. For this case, we find

$$A = 1, \tag{B25}$$

$$B = \left[\frac{(\mathbf{k}\cdot\mathbf{B}_{01})^2}{\rho_{02}\mu_0}\coth kh_1 + \frac{(\mathbf{k}\cdot\mathbf{B}_{03})^2}{\rho_{02}\mu_0}\coth kh_3\right]\coth k\Delta, \tag{B26}$$

$$C = \left(\frac{(\mathbf{k}\cdot\mathbf{B}_{01})^2}{\rho_{02}\mu_0}\coth kh_1 - kg\right)\left(\frac{(\mathbf{k}\cdot\mathbf{B}_{03})^2}{\rho_{02}\mu_0}\coth kh_3 + kg\right). \tag{B27}$$

Note $\rho_{0i}(\mathbf{k}\cdot\mathbf{V}_{Ai})^2 = (\mathbf{k}\cdot\mathbf{B}_{0i})^2/\mu_0$ has been used in deriving Eqs. (B26) and (B27) when $\rho_{0i}\to 0$. Since $B > 0$ in Eq. (B26), MRT exists if and only if $C < 0$; and the cases for $g > 0$ and $g < 0$ in Eq. (B27) were discussed in some details in Ref. 8.

[1]E. G. Harris, "Rayleigh Taylor instabilities of a collapsing cylindrical shell in a magnetic field," Phys. Fluids **5**, 1057 (1962).

[2]M. Kruskal and M. Schwarzschild, "Some instabilities of a completely ionized plasma," Proc. R. Soc. London, Ser. A **223**, 348 (1954).

[3]S. Chandrasekhar, *Hydrodynamic and Hydromagnetic Stability* (Oxford University Press, London, 1961), p. 429.

[4]D. D. Ryutov, M. S. Derzon, and M. K. Matzen, "The physics of fast Z pinches," Rev. Mod. Phys. **72**, 167 (2000).

[5]D. L. Peterson, R. L. Bowers, W. Matuska, K. D. McLenithan, G. A. Chandler, C. Deeney, M. S. Derzon, M. R. Douglas, M. K. Matzen, T. J. Nash, R. B. Spielman, K. W. Struve, W. A. Stygar, and N. F. Roderick, Phys. Plasmas **6**, 2178 (1999).

[6]D. B. Sinars, S. A. Slutz, M. C. Herrmann, R. D. McBride, M. E. Cuneo, K. J. Peterson, R. A. Vesey, C. Nakhleh, B. E. Blue, K. Killebrew, D. Schroen, K. Tomlinson, A. D. Edens, M. R. Lopez, I. C. Smith, J. Shores, V. Bigman, G. R. Bennett, B. W. Atherton, M. Savage, W. A. Stygar, G. T. Leifeste, and J. L. Porter, Phys. Rev. Lett. **105**, 185001 (2010).

[7]D. B. Sinars, S. A. Slutz, M. C. Herrmann, R. D. McBride, M. E. Cuneo, C. A. Jennings, J. P. Chittenden, A. L. Velikovich, K. J. Peterson, R. A. Vesey, C. Nakhleh, E. M. Waisman, B. E. Blue, K. Killebrew, D. Schroen, K. Tomlinson, A. D. Edens, M. R. Lopez, I. C. Smith, J. Shores, V. Bigman, G. R. Bennett, B. W. Atherton, M. Savage, W. A. Stygar, G. T. Leifeste, and J. L. Porter, Phys. Plasmas **18**, 056301 (2011).

[8]Y. Y. Lau, J. C. Zier, I. M. Rittersdorf, M. R. Weis, and R. M. Gilgenbach, Phys. Rev. E **83**, 066405 (2011).

[9]D. D. Ryutov, Phys. Plasmas **18**, 064509 (2011).

[10]J. C. Zier, Ph.D. dissertation, University of Michigan, Ann Arbor, 2010.

[11]J. C. Zier, R. M. Gilgenbach, D. A. Chalenski, Y. Y. Lau, D. M. French, M. R. Gomez, S. G. Patel, I. M. Rittersdorf, A. M. Steiner, M. Weis, P. Zhang, M. Mazarakis, M. E. Cuneo, and M. Lopez, Phys. Plasmas **19**, 032701 (2012).

[12]P. Zhang, Y. Y. Lau, I. M. Rittersdorf, M. R. Weis, R. M. Gilgenbach, D. Chalenski, and S. Slutz, "Effects of magnetic shear on the magneto-Rayleigh-Taylor instability," Phys. Plasmas **19**, 022703 (2012).

[13]R. C. Kirkpatrick, I. R. Lindemuth, and M. S. Ward, Fusion Technol. **27**, 201 (1995); I. R. Lindemuth and R. C. Kirkpatrick, Nucl. Fusion **23**, 263 (1983).

[14]R. E. Sieman, I. R. Lindemuth, and K. F. Schoenberg, Comments Plasma Phys. Controlled Fusion **18**, 363 (1999), see http://fusionenergy.lanl.gov/Documents/MTF/Why_MTF/Why-MTF-Comments.html.

[15]I. R. Lindemuth, R. E. Reinovsky, R. E. Chrien, J. M. Christian, C. A. Ekdahl, J. H. Goforth, R. C. Haight, G. Idzorek, N. S. King, R. C. Kirkpatrick, R. E. Larson, G. L. Morgan, B. W. Olinger, H. Oona, P. T. Sheehey, J. S. Shlachter, R. C. Smith, L. R. Veeser, B. J. Warthen, S. M. Younger, V. K. Chernyshev, V. N. Mokhov, A. N. Demin, Y. N. Dolin, S. F. Garanin, V. A. Ivanov, V. P. Korchagin, O. D. Mikhailov, I. V. Morozov, S. V. Pak, E. S. Pavlovskii, N. Y. Seleznev, A. N. Skobelev, G. I. Volkov, and V. A. Yakubov, Phys. Rev. Lett. **75**, 1953 (1995).

[16]T. Intrator, M. Taccetti, D. A. Clark, J. H. Degnan, D. Gale, S. Coffey, J. Garcia, P. Rodriguez, W. Sommars, B. Marshall, F. Wysocki, R. Siemon, R. Faehl, R. Forman, R. Bartlett, T. Cavazos, R. J. Faehl, K. Forman, M. H. Frese, D. Fulton, J. C. Gueits, T. W. Hussey, R. Kirkpatrick, G. F. Kiuttu, F. M. Lehr, J. D. Letterio, I. Lindemuth, W. McCullough, R. Moses, R. E. Peterkin, R. E. Reinovsky, N. F. Roderick, E. L. Ruden, K. F. Schoenberg, D. Scudder, J. Shlachter, and G. A. Wurden, Nucl. Fusion **42**, 211 (2002).

[17]M. K. Matzen *et al.*, Plasma Phys. Controlled Fusion **41**, A175 (1999).

[18]R. L. Bowers, G. Nakafuji, S. E. Greene *et al.*, Phys. Plasmas **3**, 3448 (1996); T. W. Hussey, N. F. Roderick, U. Shumlak *et al.*, Phys. Plasma **2**, 2055 (1995).

[19]S. A. Pikuz, D. B. Sinars, T. A. Shelkovenko, K. M. Chandler, D. A. Hammer, G. V. Ivanenkov, W. Stepniewski, and I. Yu. Skobelev, Phys. Rev. Lett. **89**, 035003 (2002).

[20]S. V. Lebedev, F. N. Beg, S. N. Bland, J. P. Chittenden, A. E. Dangor, M. G. Haines, K. H. Kwek, S. A. Pikuz, and T. A. Shelkovenko, Phys. Plasmas **8**, 3734 (2001).

[21]V. L. Kantsyrev, L. I. Rudakov, A. S. Safronova, A. L. Velikovich, V. V. Ivanov, C. A. Coverdale, B. Jones, P. D. LePell, D. J. Ampleford, C. Deeney, A. S. Chuvatin, K. Williamson, I. Shrestha, N. Ouart, M. F. Yilmaz, G. Osborne, A. Haboub, S. Batie, A. Astanovitsky, B. LeGalloudec, V. Nalajala, W. McDaniel, V. Shlyaptseva, T. Adkins, and C. Meyer, High Energy Density Phys. **3**(1–2), 136 (2007).

[22]R. W. Lemke, M. D. Knudson, A. C. Robinson, T. A. Haill, K. W. Struve, J. R. Asay, and T. A. Mehlhorn, "Self-consistent, two-dimensional, magnetohydrodynamic simulations of magnetically driven flyer plates," Phys. Plasmas **10**, 1867 (2003); and references therein.

[23]R. W. Lemke, M. D. Knudson, C. A. Hall, T. A. Haill, P. M. Desjarlais, J. R. Asay, and T. A. Mehlhorn, "Characterization of magnetically accelerated flyer plates," Phys. Plasmas **10**, 1092 (2003).

[24]J. Eggert, "Isentropic compression equation of state analysis," in 14th APS Topical Conference on Shock Compression of Condensed Matter,

Baltimore, MD, August 2005; T. D. Pointon, H. C. Harjes, M. E. Savage, D. E. Bliss, and R. W. Lemke, "Pulse shaping of the load current on the Z accelerator," in 2003 IEEE International Pulsed Power Conference, Dallas, Texas, IEEE Cat. No. 03CH37272, 2003.

[25]J. J. Hester, J. M. Stone, P. A. Scowen, B.-I. Jun, J. S. Gallagher III, M. L. Norman, G. E. Ballester, C. J. Burrows, S. Casertano, J. T. Clarke, D. Crisp, R. E. Griffiths, J. G. Hoessel, J. A. Holtzman, J. Krist, J. R. Mould, R. Sankrit, K. R. Stapelfeldt, J. T. Trauger, A. Watson, and J. A. Westphal, "WFPC2 studies of the crab Nebula. III. Magnetic Rayleigh-Taylor instabilities and the origin of the filaments," Astrophys. J. **456**, 225 (1996).

[26]S. A. Slutz, M. C. Herrmann, R. A. Vesey, A. B. Sefkow, D. B. Sinars, D. C. Rovang, K. J. Peterson, and M. E. Cuneo, "Pulsed-power-driven cylindrical liner implosions of laser preheated fuel magnetized with an axial field," Phys. Plasmas **17**, 056303 (2010).

[27]S. A. Slutz and R. A. Vesey, Phys. Rev. Lett. **108**, 025003 (2012).

[28]M. E. Cuneo, M. C. Herrmann, D. B. Sinars, S. A. Slutz, W. A. Stygar, R. A. Vesey, A. B. Sefkow, G. A. Rochau, G. A. Chandler, J. E. Bailey, J. L. Porter, R. D. McBride, D. C. Rovang, M. G. Mazarakis, E. P. Yu, D. C. Lamppa, K. J. Peterson, C. Nakhleh, S. B. Hansen, A. J. Lopez, M. E. Savage, C. A. Jennings, M. R. Martin, R. W. Lemke, B. W. Atherton, I. C. Smith, P. K. Rambo, M. Jones, M. R. Lopez, P. J. Christenson, M. A. Sweeney, B. Jones, L. A. McPherson, E. Harding, M. R. Gomez, P. F. Knapp, T. J. Awe, R. J. Leeper, C. L. Ruiz, G. W. Cooper, K. D. Hahn, J. McKenney, A. C. Owen, G. R. McKee, G. T. Leifeste, D. J. Ampleford, E. M. Waisman, A. Harvey-Thompson, R. J. Kaye, M. H. Hess, S. E. Rosenthal, and M. K. Matzen, IEEE Trans. Plasma Sci. **40**, 3222 (2012).

[29]D. D. Ryutov, M. E. Cuneo, M. C. Herrmann, D. B. Sinars, and S. A. Slutz, Phys. Plasmas **19**, 062706 (2012).

[30]T. J. Awe, R. D. McBride, C. A. Jennings, D. C. Lamppa, M. R. Martin, D. C. Rovang, S. A. Slutz, M. E. Cuneo, A. C. Owen, D. B. Sinars, K. Tomlinson, M. R. Gomez, S. B. Hansen, M. C. Herrmann, J. L. McKenney, C. Nakhleh, G. K. Robertson, G. A. Rochau, M. E. Savage, D. G. Schroen, and W. A. Stygar, Phys. Rev. Lett. **111**, 235005 (2013); W. W. Gibbs, Nature **505**, 9 (2014).

[31]T. J. Awe, C. A. Jennings, R. D. McBride, M. E. Cuneo, D. C. Lamppa, M. R. Martin, D. C. Rovang, D. B. Sinars, S. A. Slutz, A. C. Owen, K. Tomlinson, M. R. Gomez, S. B. Hansen, M. C. Herrmann, M. C. Jones, J. L. McKenney, G. K. Robertson, G. A. Rochau, M. E. Savage, D. G. Schroen, and W. A. Stygar, Phys. Plasmas **21**, 056303 (2014).

[32]G. I. Taylor, Proc. R. Soc. London, Ser. A **201**, 192 (1950).

[33]S. Atzeni and J. Meyer-Ter-Vehn, *The Physics of Inertial Fusion* (Oxford University Press, NY, 2004), p. 253.

[34]J. M. Koning, G. D. Kerbel, and M. M. Marinak, The Hydra Magnetohydrodynamics Package, APS-DPP, 2009; M. M. Marinak, G. Kerbel, N. Gentile, O. Jones, D. Munro, S. Pollaine, T. R. Dittrich, and S. W. Haan, Phys. Plasmas **8**, 2275 (2001).

[35]G. I. Bell, "Taylor instability on cylinders and spheres in the small amplitude approximation," Los Alamos Scientific Laboratory, Report LA-1321, 1951.

[36]M. S. Plesset, J. Appl. Phys. **25**, 96 (1954).

[37]P. M. Bellan, *Fundamentals of Plasma Physics* (Cambridge University Press, 2006).

[38]J. R. Melcher, *Continuum Mechanics* (MIT Press, Cambridge, MA, 1981).

[39]K. J. Peterson, D. B. Sinars, E. P. Yu, M. C. Herrmann, M. E. Cuneo, S. A. Slutz, I. C. Smith, B. W. Atherton, M. D. Knudson, and C. Nakhleh, Phys. Plasmas **19**, 092701 (2012).

[40]K. J. Peterson, E. P. Yu, D. B. Sinars, M. E. Cuneo, S. A. Slutz, J. M. Koning, M. M. Marinak, C. Nakhleh, and M. C. Herrmann, Phys. Plasmas **20**, 056305 (2013).

[41]K. J. Peterson, T. J. Awe, E. P. Yu, D. B. Sinars, E. S. Field, M. E. Cuneo, M. C. Herrmann, M. Savage, D. Schroen, K. Tomlinson, and C. Nakhleh, Phys. Rev. Lett. **112**, 135002 (2014).

[42]K. S. Holian, "T-4 handbook of material properties data bases," Los Alamos Laboratory, Report No. LA-10160-MS, 1984.

[43]M. P. Desjarlais, Contrib. Plasma Phys. **41**, 267 (2001).

[44]J. J. MacFarlane, I. E. Golovkin, P. Wang, P. R. Woodruff, and N. A. Pereyra, "SPECT3D—A multi-dimensional collisional-radiative code for generating diagnostic signatures based on hydrodynamics and PIC simulation output," High Energy Density Phys. **3**, 181 (2007).

[45]G. R. Bennett, I. C. Smith, J. E. Shores, D. B. Sinars, G. Robertson, B. W. Atherton, M. C. Jones, and J. L. Porter, Rev. Sci. Instrum. **79**, 10E914 (2008).

[46]A. S. Gilmour, *Microwave Tubes, Artch House* (Norwood, MA, 1986).

[47]E. P. Yu, M. E. Cuneo, M. P. Desjarlais, R. W. Lemke, D. B. Sinars, T. A. Haill, E. M. Waisman, G. R. Bennett, C. A. Jennings, T. A. Mehlhorn, T. A. Brunner, H. L. Hanshaw, J. L. Porter, W. A. Stygar, and L. I. Rudakov, Phys. Plasmas **15**, 056301 (2008).

[48]M. R. Martin, R. W. Lemke, R. D. McBride, J. P. Davis, D. H. Dolan, M. D. Knudson, K. R. Cochrane, D. B. Sinars, I. C. Smith, M. Savage, W. A. Stygar, K. Killebrew, D. G. Flicker, and M. C. Herrmann, Phys. Plasmas **19**, 056310 (2012).

[49]H. P. Furth, J. Killeen, and M. N. Rosenbluth, Phys. Fluids **6**, 459 (1963).